



AFRL-RW-EG-TR-2013-080

VOID GROWTH AND COALESCENCE SIMULATIONS

Derek J. Reding¹
Pavol Stofko²
Robert J. Dorgan³
Michael E. Nixon⁴

¹ Jacobs TEAS Team
1030 Titan Court
Fort Walton Beach, Florida 32547

² Armament Research Development & Engineering Center
Picatinny Arsenal, New Jersey 07806

³ Air Force Research Laboratory, Munitions Directorate
101 West Eglin Blvd.
Eglin Air Force Base, Florida 32542

⁴ Applied Research Associates, Emerald Coast Division
956 West John Sims Parkway
Niceville, Florida 32578

AFOSR LRIR 12RW04COR

AUGUST 2013

INTERIM REPORT

DISTRIBUTION A. Approved for public release, distribution unlimited. (96ABW-2013-0310)

**AIR FORCE RESEARCH LABORATORY
MUNITIONS DIRECTORATE**

■ Air Force Materiel Command

■ United States Air Force

■ Eglin Air Force Base, FL 32542

NOTICE AND SIGNATURE PAGE

Using Government drawings, specifications, or other data included in this document for any purpose other than Government procurement does not in any obligate the U.S. Government. The fact that the Government formulated or supplied the drawings, specifications, or other data does not license the holder or any other person or corporation, or convey any rights or permission to manufacture, use, or sell any patented invention that may relate to them.

This report was cleared for public release by the 96th Air Base Wing, Public Affairs Office, and is available to the general public, including foreign nationals. Copies may be obtained from the Defense Technical Information Center (DTIC) < <http://www.dtic.mil/dtic/index/html>>.

AFRL-RW-EG-TR-080 HAS BEEN REVIEWED AND IS APPROVED FOR PUBLICATION IN ACCORDANCE WITH ASSIGNED DISTRIBUTION STATEMENT.

FOR THE DIRECTOR:

SIGNED

Craig R. Ewing, DR-IV, PhD
Technical Advisor
Weapon Engagement Division

SIGNED

Robert J. Dorgan
Senior Research Scientist
Computational Mechanics Branch

This report is published in the interest of scientific and technical information exchange, and its publication does not constitute the Government's approval or disapproval of its ideas or findings.

REPORT DOCUMENTATION PAGE

*Form Approved
OMB No. 0704-0188*

The public reporting burden for this collection of information is estimated to average 1 hour per response, including the time for reviewing instructions, searching existing data sources, gathering and maintaining the data needed, and completing and reviewing the collection of information. Send comments regarding this burden estimate or any other aspect of this collection of information, including suggestions for reducing the burden, to Department of Defense, Washington Headquarters Services, Directorate for Information Operations and Reports (0704-0188), 1215 Jefferson Davis Highway, Suite 1204, Arlington, VA 22202-4302. Respondents should be aware that notwithstanding any other provision of law, no person shall be subject to any penalty for failing to comply with a collection of information if it does not display a currently valid OMB control number.

PLEASE DO NOT RETURN YOUR FORM TO THE ABOVE ADDRESS.

1. REPORT DATE (DD-MM-YYYY) 06-08-2013	2. REPORT TYPE INTERIM REPORT	3. DATES COVERED (From - To) 31-10-2011 - 01-06-2013
--	---	--

4. TITLE AND SUBTITLE VOID GROWTH AND COALESCENCE SIMULATIONS	5a. CONTRACT NUMBER N/A
	5b. GRANT NUMBER N/A
	5c. PROGRAM ELEMENT NUMBER 3002

6. AUTHOR(S) Derek J. Reding 1 Pavol Stofko 2 Robert J. Dorgan 3 Michael E. Nixon 4	5d. PROJECT NUMBER
	5e. TASK NUMBER
	5f. WORK UNIT NUMBER W0AQ

7. PERFORMING ORGANIZATION NAME(S) AND ADDRESS(ES) 1 Jacobs TEAS Team; 1030 Titan Court; Fort Walton Beach, FL 32547 2 ARDEC; Picatinny Arsenal, New Jersey 07806 3 AFRL; 101 West Eglin Blvd.; Eglin AFB, Florida 32542 4 Applied Research Associates, ECD; 956 W. John Sims Pkwy, Niceville, FL 32578	8. PERFORMING ORGANIZATION REPORT NUMBER AFRL-RW-EG-TR-2013-080
--	---

9. SPONSORING/MONITORING AGENCY NAME(S) AND ADDRESS(ES) Air Force Research Laboratory, Munitions Directorate AFRL/RWWC 101 West Eglin Blvd. Eglin AFB, Florida 32542	10. SPONSOR/MONITOR'S ACRONYM(S) AFRL/RW
	11. SPONSOR/MONITOR'S REPORT NUMBER(S) AFRL-RW-EG-TR-2013-080

12. DISTRIBUTION/AVAILABILITY STATEMENT
DISTRIBUTION A. Approved for public release, distribution unlimited. (96ABW-2013-0310)

13. SUPPLEMENTARY NOTES

14. ABSTRACT
Recent experiments, in which voids are precision cut using a second laser, have been used to study void coalescence. In that study, both the Rice and Tracey model and the Thomason model were shown to have reasonable agreement with experiment results for the copper, in most cases. However, no simulations were performed in which voids were explicitly represented. This article uses finite element simulations to describe void coalescence as observed in copper bar uniaxial tension experiments. Several problems occur when meshing the three-dimensional geometry containing 176 voids, namely element distortion and damage, minimum time step, and appropriate material model parameters. Further, a temporal and spatial convergence study was used to estimate errors, thus, this study helps to provide guidelines for modeling of materials with voids. Finally, we use a Gurson model with Johnson-Cook strength to simulate the void growth. Simulations, using the codes ABAQUS explicit, EPIC, and Presto, agree well with experiments.

15. SUBJECT TERMS
Coalescence; Fracture; Simulations; Damage Modeling

16. SECURITY CLASSIFICATION OF:			17. LIMITATION OF ABSTRACT UL	18. NUMBER OF PAGES	19a. NAME OF RESPONSIBLE PERSON ROBERT J. DORGAN
a. REPORT UNCLAS	b. ABSTRACT UNCLAS	c. THIS PAGE UNCLAS			19b. TELEPHONE NUMBER (Include area code) 850-882-3124

Reset

TABLE OF CONTENTS

Section	Page
TABLE OF CONTENTS.....	i
TABLE OF FIGURES.....	ii
TABLE OF TABLES.....	ii
ACKNOWLEDGEMENTS.....	iii
1.0 SUMMARY.....	1
2.0 INTRODUCTION.....	1
3.0 METHODS, ASSUMPTIONS, AND PROCEDURES.....	2
3.1 Void Coalescence.....	2
3.2 Code Verification.....	2
3.3 Verification Approach.....	3
3.3.1 Models of Convergence Error.....	3
3.3.2 Grid Convergence Study.....	5
3.4 Macroscopic Modeling.....	5
3.5 Finite Element Simulations.....	6
4.0 RESULTS AND DISCUSSIONS.....	11
5.0 CONCLUSIONS.....	15
6.0 REFERENCES.....	16

TABLE OF FIGURES

Figure 1: Uniaxial Tension Specimen (a) Actual Specimen; (b) Gage Length	7
Figure 2: Laser Drilled Rectangular Array of 176 holes (only partially shown) Oriented at 45° to the Tensile Axis	7
Figure 3: Uniaxial Tension Specimen (Model 3)	9
Figure 4: Uniaxial Tension Specimen of the Coarsest Mesh (Model 3). (a) Full Model of Specimen; (b) Close up of the Cross-Section of the Porous Region	10
Figure 5: Dimensions of Continuum Void Region	10
Figure 6: True stress vs. true strain Weck's experiment	12
Figure 7: Stress vs. Strain for Abaqus Simulations.	13
Figure 8: Stress vs. Strain for Presto Simulations	13
Figure 9: Stress vs. Strain for EPIC Simulations	14
Figure 10: Abaqus Void Visualization vs. Experiment at 0% True Strain in (a) and (b), and at 50% True Strain in (c) and (d)	15

TABLE OF TABLES

Table 1: Mesh Refinement Summary	9
Table 2: Mesh Dependency Summary (OFHC Copper)	11
Table 3: Convergence Study, L = low ($r_h = 2.187$), H = high ($r_h = 2.329$)	12
Table 4: Simulation Run Times	12

ACKNOWLEDGEMENTS

This research has been supported by Dr. David Stargel, Air Force Office of Scientific Research (AFOSR) under Laboratory Research Initiation Request (LRIR) 12RW04COR.

1.0 SUMMARY

Recent experiments, in which voids are precision cut using a second laser, have been used to study void coalescence. In that study, both the Rice and Tracey model and the Thomason model were shown to have reasonable agreement with experiment results for the copper, in most cases. However, no simulations were performed in which voids were explicitly represented. This article uses finite element simulations to describe void coalescence as observed in copper bar uniaxial tension experiments. Several problems occur when meshing the three-dimensional geometry containing 176 voids, namely element distortion and damage, minimum time step, and appropriate material model parameters. Further, a temporal and spatial convergence study was used to estimate errors, thus, this study helps to provide guidelines for modeling of materials with voids. Finally, we use a Gurson model with Johnson-Cook strength to simulate the void growth. Simulations, using the codes ABAQUS explicit, EPIC, and Presto, agree well with experiments.

Keywords: Coalescence; Fracture; Simulations; Damage Modeling

2.0 INTRODUCTION

Damage, in solid mechanics, is the state of a material which has lost structural integrity or other mechanical properties of interest. Material damage can involve void coalescence. This may be especially true for ductile fracture mechanisms (see for example ref. [1]). Ductile type fracture behavior may occur when shear bands form, especially at elevated strain rates as observed in the Kalthoff experiment [2], which is an experiment that is challenging to simulate due to the difficulty of correctly modeling damage.

Damage can involve void nucleation, growth, and coalescence, which are physical phenomena that require high resolution computational approaches for simulation. Experiments used to study these physical phenomena include gas-gun, expanding ring fragmentation, penetration, and perforation or plugging. The range of length scales needed to span void nucleation and crack formation are on the order of 10^4 (micrometers to centimeters). Cracks that have formed may grow, bifurcate, merge with other cracks, or arrest.

To visualize void growth and coalescence in a controlled manner, Weck et al. [3] experimented with model materials that contain laser-drilled holes. Void growth and coalescence were observed via X-ray tomography with impressive resolution. This behavior is important when attempting to understand damage evolution. The tensile test that was used is sufficient to examine stress triaxiality and local plastic behavior, which both help to isolate the relevant physics for a relatively simple experiment. Therefore, this experiment was selected as an appropriate benchmark problem.

We are motivated to simulate void growth and coalescence to validate codes 1) to better validate continuum void growth models, 2) to know what computational strategy will best simulate the physics, and 3) to better understand the limitations of our codes. The nearly pure copper material is used in this article because we have Johnson-Cook model parameters. Moreover, pure copper is a ductile metal with many applications in which damage occurs.

3.0 METHODS, ASSUMPTIONS, AND PROCEDURES

3.1 Void Coalescence

Void coalescence has been modeled at the macroscale continuum level by several authors [4], [5], [6], [7], [8], [9]. Tonks et al. incorporated void linking via an intervoid ligament as a basic mechanism that was used to model the local instability [4]. Kim et al. [5] studied the effects of stress triaxiality on void coalescence using the Gurson-Tvergaard constitutive relation. Another Gurston-type approach was proposed by Lassance et al. [6] and used to study penny-shaped voids resulting from particle fracture. Void nucleation, growth and coalescence were modeled by Hammi and Horstemeyer [7] using an anisotropic damage progression formulation, in which coalescence was modeled as a second rank tensor that is governed by the plastic strain rate tensor and the stress state, where the coalescence threshold is related to the void length scale. Maire et al. [8] modeled their uniaxial tension experiments using the classical Rice and Tracey approach [10] and later Landron et al. [9] used the Rice and Tracey approach that was corrected by Huang [11]. In the later article, cavity shape change was incorporated and used to improve model fits to experiment results.

Finite element simulations of void coalescence were performed by some of the aforementioned authors. Kim et al. [5] presented a finite element approach that included a representative unit cell containing a spherical void at its center. Lassance et al. [6] studied a three dimensional periodic packing of voids by a cylinder with appropriate boundary conditions. In that study, void coalescence was possible before necking in a purely uniaxial tension condition, provided that the initial void volume fraction was sufficiently high. Several other authors have simulated a single pore geometry using finite elements. In one of the more recent studies, Siad et al. [12] studied void coalescence, but with a sole focus on finite element simulations of a single cylindrical void geometry. Ha and Kim [13] investigated void growth and coalescence in an anisotropic crystalline material, namely f.c.c. single crystals, using the finite element method. In their study, the growth and coalescence behavior were simulated using a single pore.

Previous void coalescence experiments have been conducted. See for example, the non-destructive X-ray tomography experiments in refs. [3], [8], [9]. Recent experiments by Weck [3] isolate void growth and coalescence in a controlled manner via laser-drilled holes. In contrast, natural void evolution and coalescence was observed by Landron et al. [9], where damage evolution in dual-phase steel was studied [8], [9]. In the latter study, the correction by Huang [11] to the Rice and Tracey model [10] was validated for different triaxiality states.

3.2 Code Verification

Verification is the process of determining that a model implementation accurately represents the developer's conceptual description of the model and the solution to the model [14]. Four predominant sources of error are 1) insufficient spatial discretization convergence, 2) insufficient temporal discretization convergence, 3) lack of iterative convergence, and 4) computer programming [15]. Programming errors and iterative convergence are not addressed in this paper. The solution over the entire computational domain, including boundaries, must be verified for the geometry and loading conditions of interest.

None of the previous studies mentioned here included an explicit mesh for multiple voids. Moreover, void coalescence was not simulated for an experimental geometry that included voids. Instead, the aforementioned studies focused on meshing a single void, and in one case, periodic boundary conditions were used [6]. These studies only used one mesh and the largest allowable time step, thus, neither spatial nor temporal refinements were used. Therefore, this article is the first to attempt to quantify spatial and temporal convergence rates, asymptotic regime, and corresponding errors. These activities are part of uncertainty quantification, which addresses the three fundamental components of computer simulations for physical systems, namely, model qualification, model verification, and model validation [14]. Although previous penetration studies are strong in model qualification, model validation is impossible without complete verification, i. e. numerical error quantification.

The grid convergence index (GCI) is a relatively simple method to estimate errors due to mesh refinements. However, GCI methods cannot provide statistical confidence, which can be obtained using response surface methods (RSM) [16]. Another limitation for GCI methods is the use of an empirical safety factor F_s to provide a confidence interval. Some of the assumptions made in the GCI and RSM methods are relaxed in a nonlinear ansatz error model [17].

Confidence estimation for a given safety factor is based on the number of grid points used N_g and no consensus has been reached on the value. Approximately 95% certainty (5% uncertainty, that is roughly a 2σ error band if the distribution is Gaussian) is assumed for $N_g \geq 3$, and $F_s = 1.25$ [18]. Although these values are for steady state fluid flow and heat transfer, they are commonly used in a wide range of hydrocode verification studies. A consensus has been reached that multiple methods should be explored in a systematic verification study and that GCI methods ($N_g \geq 3$) often produce useful information. For example, relative GCI values for different grid sets were used in Ref. [19] to determine the best grid set based on finding the lowest GCI.

3.3 Verification Approach

Verification involves quantifying the error associated with solving the governing equations regardless of the values of the model parameters. The most important part of verification is to perform spatial and temporal refinement studies.

The first step is to identify the metrics or quantities of interest for observing convergence, namely 1) displacement (Δ_c) and 2) load or force (L_c), at the end of the bar at which point voids coalesce. Experiments described above provide accelerometer data and penetration depth. Therefore, penetration depth is considered to be the most important verification metric in this study.

3.3.1 Models of Convergence Error.

The exact solution is denoted as F^* and discrete solutions are denoted in simplified notation, $F_{x,t} = F(\Delta x, \Delta t)$. We define the general error metric in Eq. (1) using the norm of the difference between the continuous and numerical solutions:

$$e_{x,t} = \|F^* - F_{x,t}\| \quad (1)$$

For the metrics used in this paper, the error is simply the absolute value of the difference, that is, $e_{x,t} = |F^* - F_{x,t}|$.

Discretized solutions that neglect higher order terms according to the Richardson extrapolation estimation (REE) technique are given by,

$$F_{x,t} = F^* + \alpha^* h_i^{p^*} \quad (2)$$

where α^* is a fitting constant, p^* is the convergence rate or order of convergence, and h_i is either the spatial or temporal step size, $1/N_{cells}$. Equation (2) is rarely if ever observed in practice. Alternatively, the approximate solution \tilde{F} approximates F^* by extrapolation such as the REE technique or by response surface methods. Therefore, we can approximate Eq. (2) by,

$$F_{x,t} = \tilde{F} + \tilde{\alpha} h_i^{\tilde{p}} \quad (3)$$

where the REE fitting parameters are $\{\tilde{\lambda}, \tilde{\alpha}, \tilde{p}\}$. The corresponding space-only or time-only error estimation is given by,

$$e_{x,t} = \tilde{\lambda}_0 + \tilde{\alpha} h_i^{\tilde{p}} + h. o. t. \quad (4)$$

Higher order terms (*h. o. t.*) are neglected in this three parameter fit with parameters $\{\tilde{\lambda}_0, \tilde{\alpha}, \tilde{p}\}$.

The asymptotic region is described in this study to be the set of spatial and temporal mesh sizes that provide a consistent and accurate order of convergence and GCI. This region is generally unknown before performing simulations. An estimated order of convergence may be calculated using three grid points $N_g = 3$, constant refinement ratio r_h , constant α , and constant convergence rate p , as in Roache [20], as

$$\tilde{p}_r = \log \left[\frac{(F_1 - F_3)}{(F_1 - F_2)} \right] / \log[r_h] \quad (5)$$

where F_1 , F_2 , and F_3 are the fine, medium, and coarse grid solutions, respectively. If the grid convergence is monotonic with constant convergence rate, then $\tilde{p}_r = p^*$ and the extrapolated solution is given by,

$$\tilde{F} = F^* = F_1 + \frac{(F_1 + F_2)}{(r_h^{\tilde{p}_r} - 1)} \quad (6)$$

However, $\tilde{F} = F^*$ is generally not true. Further, \tilde{p} and $\tilde{\alpha}$ are rarely constant. A safety factor F_s is used to provide the GCI, which is expressed as

$$GCI = F_s \left| \frac{F_1 - F_2}{F_1} \right| / (r_h^{\tilde{p}_r} - 1) \quad (7)$$

A conservative safety factor $F_s = 3$ is used with $N_g = 3$ is assumed to estimate the uncertainty 68% of the time (or 1σ) because we assume a Gaussian error distribution.

Three main assumptions are made in the formulation above. The error according to Eq. (4) assumes that, 1) numerical solution convergence is monotonic, 2) space-time coupling effects are neglected, and 3) higher order terms are negligible.

Coefficients in Eq. (4) are solved analytically as in Eq. (5). Throughout this paper, we use the following error definition:

$$\tilde{e}_{x,t} = \tilde{F} - F_{x,t} \quad (8)$$

3.3.2 Grid Convergence Study.

Several uniaxial tension simulations are used to investigate spatial and temporal refinements. The following two steps are used for the nominal case refinement study:

Extrapolate solution \tilde{F} from Eq. (6) assuming $\tilde{p} = \tilde{p}_r$.

Apply the three parameter space-only fit using Eq. (4) and optimization procedure described above.

The spatial refinement set is $dx = [W/10, W/20, W/40]$, where W is the width of the tension specimen. The temporal refinement set is $CFL = [1.0, .5, .25]$, where the Courant-Friedrichs-Lewy (CFL) is a fraction of the maximum stable time step, or in this article, the fixed time step in which mass-scaling was used. Although the CFL does not correspond directly to the time step, CFL values are appropriate for temporal refinements in tensile loading simulations because the minimum time step is determined from conditions near the edges of the pores. Therefore, pore growth and coalescence are sensitive to temporal refinements using CFL values.

The stable time step using ABAQUS was on the order of $1e-11$ seconds, which is prohibitively small even on a high performance computing cluster. Therefore, we used mass-scaling.

3.4 Macroscopic Modeling

In addition to the simulation, in which the mesh is refined such that geometry of the voids is explicitly included, we compare a macroscale damage model approach. For the EPIC code, we use the following Gurson-type yield criterion (see for example Tvergaard and Needleman [21]).

$$\Phi = \frac{\sigma_e^2}{\sigma_M^2} + 2q_1 \cosh\left(\frac{\sigma_k^k}{2\sigma_M}\right) - 1 - q_1^2 = 0 \quad (9)$$

where the macroscopic Mises stress is $\sigma_e = \left(3s_{ij}s^{ij}/2\right)^{1/2}$, in terms of the stress deviator $s_{ij} = \sigma^{ij} - G^{ij}\sigma_k^k/3$, and σ_k^k is the macroscopic mean stress. For $q_1 = 1$, Eq. (9) is that derived by Gurson [1].

A Mie-Grüneisen equation of state (EOS) is used. The pressure for the virgin material [22] is given by,

$$\tilde{P} = \tilde{P}(\tilde{\mu}, \tilde{e}) = P_H \left(1 - \frac{1}{2} \Gamma \tilde{\mu} \right) + \Gamma \tilde{\rho} \tilde{e} \quad (10)$$

where $\tilde{\rho} = \rho / (1 - \phi)$ is the density of the solid material, ϕ is the ratio of void volume over the total volume, $\tilde{e} = e$ is the internal energy of the solid material, $\tilde{\mu} = \tilde{\rho} / \tilde{\rho}_0 - 1$ is the current density ρ and the initial density ρ_0 , Γ is the Gruneisen constant for the solid material. The Hugoniot pressure consistent with the standard quadratic EOS form is given in Eq. (11) in terms of three parameters that are fit to experiments, namely k_1 , k_2 , and k_3 .

$$P_H = k_1 \tilde{\mu} + k_2 \tilde{\mu}^2 + k_3 \tilde{\mu}^3 \quad (11)$$

For EPIC, Presto, and Abaqus simulations, we used the Johnson-Cook strength model [22], which is given by,

$$\sigma = [A + B \varepsilon_p^n] [1 + C \ln \dot{\varepsilon}^*] [1 - T^{*m}] + \alpha P \quad (12)$$

where ε_p is the equivalent plastic strain, $\dot{\varepsilon}^* = \dot{\varepsilon} / \dot{\varepsilon}_o$ is the dimensionless total strain rate where $\dot{\varepsilon}$ is the equivalent total strain rate, $\dot{\varepsilon}_o = 1.0 \text{ s}^{-1}$, $T^* = (T - T_{room}) / (T_{melt} - T_{room})$ is the homologous temperature, P is the hydrostatic pressure, and A , B , n , C , m , and α are material constants [22].

3.5 Finite Element Simulations

The tensile test that was used in Ref. [3] is used here as an appropriate benchmark problem. The full tensile specimen is dimensioned in Figure 1 (a). The gage length is the portion of the specimen used in the simulations and is the 2.0 mm length shown in Figure 1 (b). The specimen with a gauge length rectangular cross section was constructed from three plates. The 10 μm middle plate had 176 holes with 10 μm diameters drilled using a laser in a rectangular array oriented at 45 $^\circ$ to the tensile axis. The center-to-center hole spacing was 20 μm , and further details of the array are shown in Figure 2.

The simulated boundary conditions are built-in ends that load the bar in uniaxial tension at a strain rate of 0.1 s^{-1} .

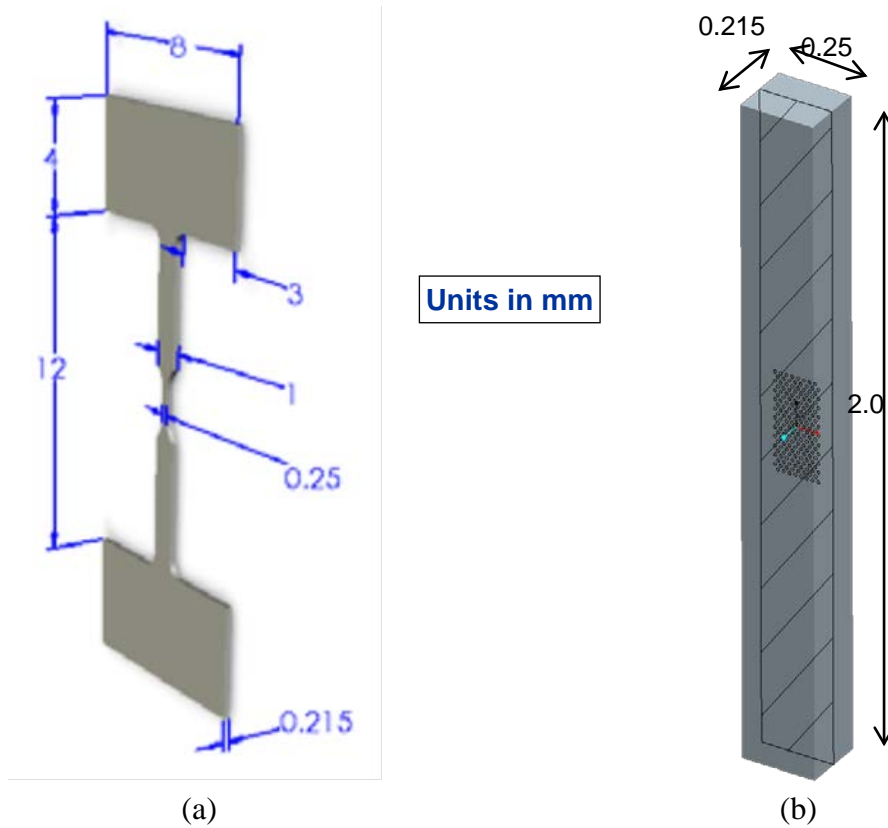


Figure 1: Uniaxial Tension Specimen (a) Actual Specimen; (b) Gage Length

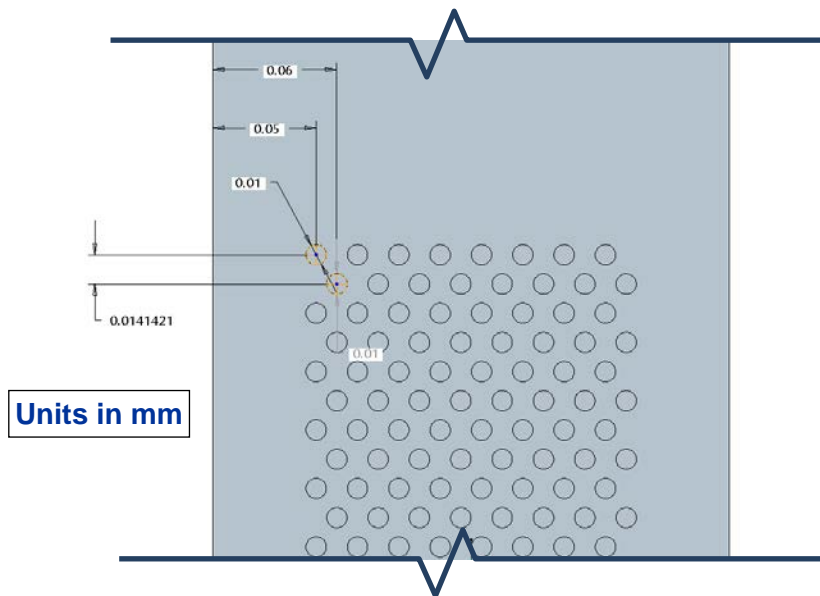


Figure 2: Laser Drilled Rectangular Array of 176 holes (only partially shown) Oriented at 45° to the Tensile Axis

The hydrocodes Abaqus [23], Presto [24], and EPIC [25] are used in the current work for their leading capabilities. These codes were used with Lagrangian implementation, appropriate constitutive models, and equation of state. Additionally, all three codes are capable of using a macroscale continuum model similar to Gurson’s model.

Abaqus and Presto both have approximately second order accuracy in space and time. Lagrangian methods in both codes are used with tetrahedron elements in this study. Further details can be found in Ref. [26] In an effort to minimize computational time, the specimen geometry was initially meshed with hexagonal elements; however, it was found to be not possible to further refine the hexagonal mesh in the porous regions. The mesh was therefore re-generated with tetrahedral elements in the porous region of the specimen only, leaving the un-porous top and bottom regions meshed with hexagonal elements. This scheme was also found problematic due to the use of a tie constraint by the hydrocodes at the transitional surfaces in order to combine the different element regions in the model. These tie constraints could introduce artificial constraints to the model, which could lead to a restraining behavior in the specimen from necking. It was decided to maintain the most realistic integrity of the model and accept the longer computational time by generating a full tetrahedron mesh of the entire specimen.

For all simulations, we used the Johnson-Cook (HJC) model [27] with Mie-Grüneisen equation of state (EOS) to model the pressure, density, and internal energy relationship. Element failure was assumed to occur when i) elements inverted, ii) nodal Jacobian ratio became negative, or iii) the element equivalent plastic strain exceeded 150%.

In Abaqus, the equivalent plastic strain rate is defined as,

$$\dot{\epsilon}^{pl} = D \left(\frac{\bar{\sigma}}{\sigma^0} - 1 \right)^n \quad \text{for } \bar{\sigma} \geq \sigma^0 \quad (13)$$

where $\bar{\sigma}$ is yield stress at nonzero strain rate, $\sigma^0(\epsilon^{pl}, \theta, f_i)$ is static yield stress, θ is temperature, f_i are other field variables, and $D(\theta, f_i)$ and $n(\theta, f_i)$ are material parameters.

Material failure or element deletion is mesh dependent. Although material failure is mesh dependent, solution convergence, if it exists, is not necessarily the same as for the conservation equations and momentum balance. Errors can be reduced by refining the mesh in locations in which material is expected to fail. Therefore, refinements were made to all elements in the simulated specimen, specifically those in the porous region where elements tend to fail first. The specimen geometry was partitioned into three regions as shown in Figure 3 below. The mesh refinement was established by decreasing the global mesh seed of the entire model. Additional refinement was performed on Region 2 of the specimen, where the refinement metric used was the number of element line segments per circular void. Table 1 below lists the refinement details for all three models generated.

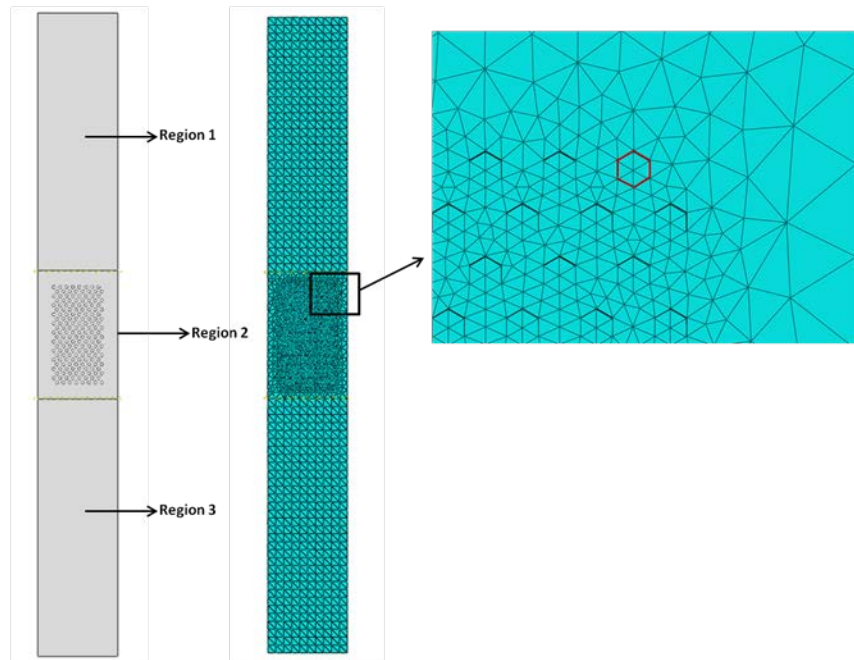


Figure 3: Uniaxial Tension Specimen (Model 3)

Table 1: Mesh Refinement Summary

Region	Model 1 (fine)		Model 2 (middle)		Model 3 (course)	
	Nodes	Elements	Nodes	Elements	Nodes	Elements
1	28,620	152,359	13,076	65,813	6,078	28,036
2	107,957	621,838	47,061	267,045	21,980	122,093
3	28,669	152,574	13,130	66,173	6,038	27,775
Totals	165,246	926,771	73,267	399,031	34,096	167,904
Void Refinement	12 Element Line Segments		8 Element Line Segments		6 Element Line Segments	

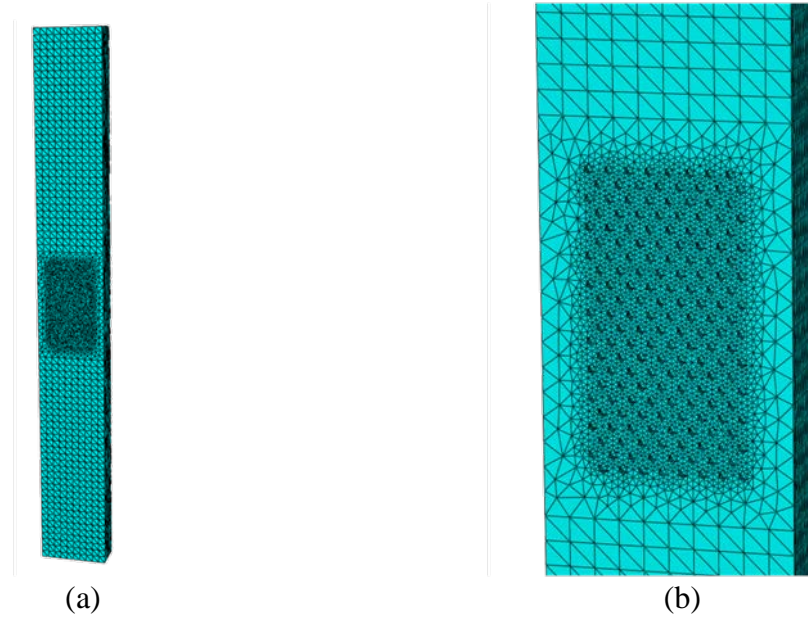


Figure 4: Uniaxial Tension Specimen of the Coarsest Mesh (Model 3). (a) Full Model of Specimen; (b) Close up of the Cross-Section of the Porous Region

The macroscale continuum void region is estimated based on the 6.5% void volume fraction specified by Weck [3]. This region has length and width approximated based on the size of rectangular void region shown in Figure 5 above. The width and height of a rectangle tangential to the outside rows of voids is 160 microns and 307 microns, respectively. A buffer region was placed around this tangential rectangle to create an approximate continuum void region with width and height of 170 microns and 311 microns, respectively. The actual voids had a through thickness of 10 microns; however, to maintain the total volume of these voids for a 6.5% void volume fraction, the thickness of this continuum void region was set to 46.3 microns.

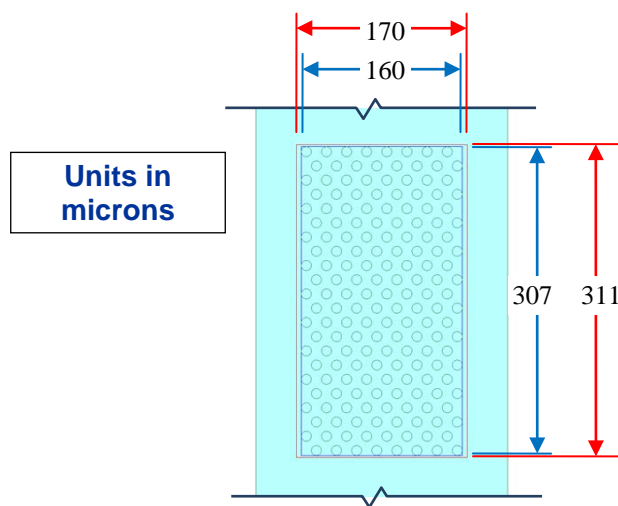


Figure 5: Dimensions of Continuum Void Region

4.0 RESULTS AND DISCUSSIONS

The following equations from Ref. [3] were used to generate results in all simulations:

$$\sigma = s(e + 1) \quad (14)$$

$$\varepsilon = \ln(e + 1) \quad (15)$$

$$\sigma = \frac{L}{A} \quad (16)$$

$$\varepsilon = \ln\left(\frac{A_0}{A}\right) \quad (17)$$

where Eqs. (14) and (15) are used to calculate true stress-strain curves prior to necking, and Eqs. (16) and (17) are used to calculate these curves after necking. In these equations, $s = L/A_0$ is the engineering stress, $e = (l - l_0)/l_0$ is the engineering strain, L is the load, A_0 is the initial cross-sectional area, and l_0 and l are the initial and current gage lengths, respectively. For the true stress vs. true strain calculations, the area in the middle of the specimen where the necking occurred was calculated by tracking the node displacements at the corners during each simulation. This tracked area was used in Eqs. (16) and (17) to compute true stress and true strain values.

Results for the two metrics are given for various mesh refinements in Table 2. From Ref. [3], the true strain at necking, $\varepsilon_n = 0.26$, $\sigma_n = 250$ MPa, is found from the intersection between the true stress and the work-hardening rate curves as a function of true strain, as shown in Figure 6.

We obtain for each metric, a) order of convergence, and b) extrapolated solution with corresponding uncertainty, and c) computation time for each simulation. Order of convergence and GCI are compared to results obtained from experiments. Convergence results and the solution uncertainty calculated for CFL values are summarized in Table 3.

Stress vs. strain curves from FEA simulations are shown in Figure 7, Figure 8, and Figure 9 for comparison with the experimental stress vs. strain curves shown in Figure 6. Note that we compare only the Copper experimental data, not Glidcop. ABAQUS simulations for Models 1, 2, and 3 are shown in Figure 7 (a), (b), and (c), respectively. Presto simulation Models 2 and 3 are shown in Figure 8 (a) and (b), respectively. Model 1 simulations for Presto were never completed due to a very large estimated run time as shown in Table 4, which was predicted after 15% of completion of the simulation. EPIC simulations for Models 1, 2, and 3 are shown in Figure 9 (a), (b), and (c), respectively.

Table 2: Mesh Dependency Summary (OFHC Copper)

dx	Abaqus		EPIC		Presto	
	ε_n	σ_n (MPa)	ε_n	σ_n (MPa)	ε_n	σ_n (MPa)
Model 1	0.2262	319.74	0.2104	310.81	--	--
Model 2	0.2271	320.64	0.2083	310.20	0.2143	314.14
Model 3	0.2282	321.39	0.2030	308.58	0.2030	314.20

Table 3: Convergence Study, L = low ($r_h = 2.187$), H = high ($r_h = 2.329$)

dx	Abaqus		EPIC	
	ϵ_n	σ_n (MPa)	ϵ_n	σ_n (MPa)
ρ_r (L/H)	1.020/0.945	0.775/0.717	1.610/1.490	1.657/1.533
F_{ext}	0.2255	318.7	0.2112	311.0
GCI	0.0098	0.0019	0.0119	0.0022

Table 4: Simulation Run Times

	Abaqus	EPIC	Presto
	run time (hrs)	run time (hrs)	run time (hrs)
Model 1	200.8	401.8	952.4
Model 2	53.3	204.9	328.1
Model 3	18.6	109.9	253.5

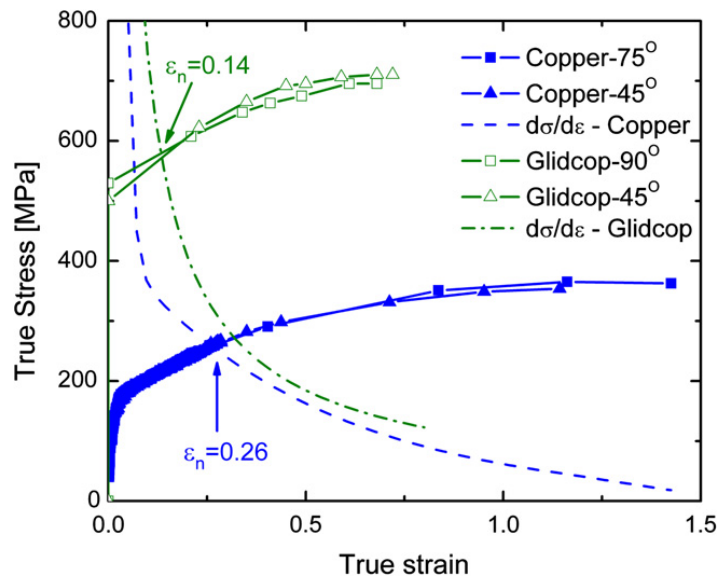
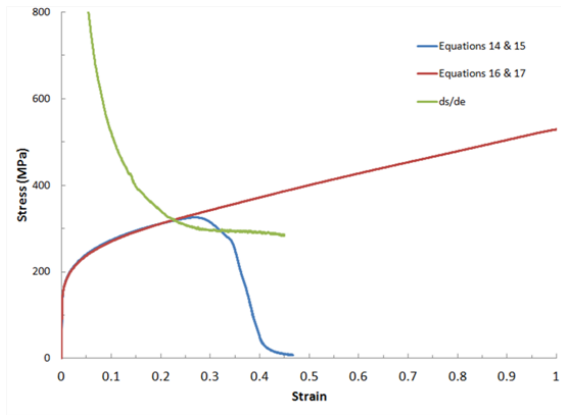
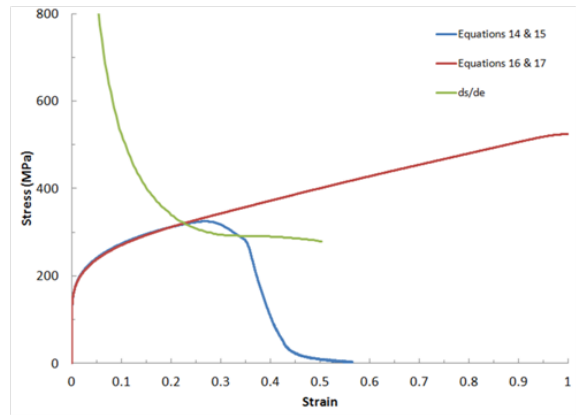


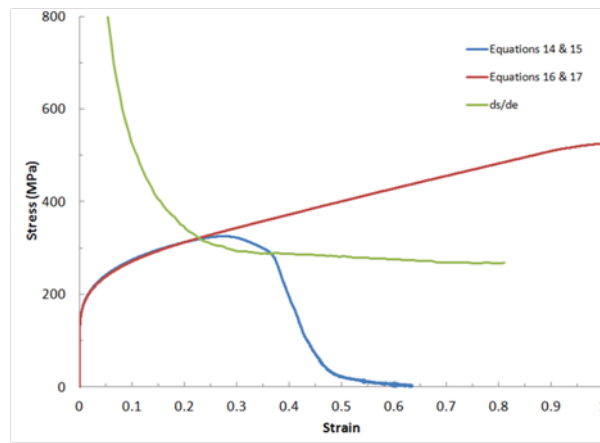
Figure 6: True stress vs. true strain Weck's experiment.



(a)

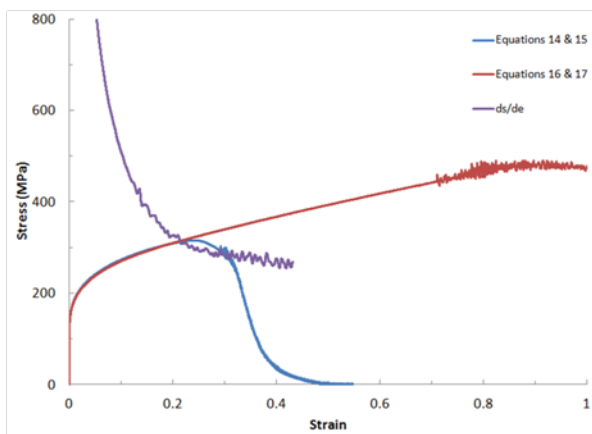


(b)

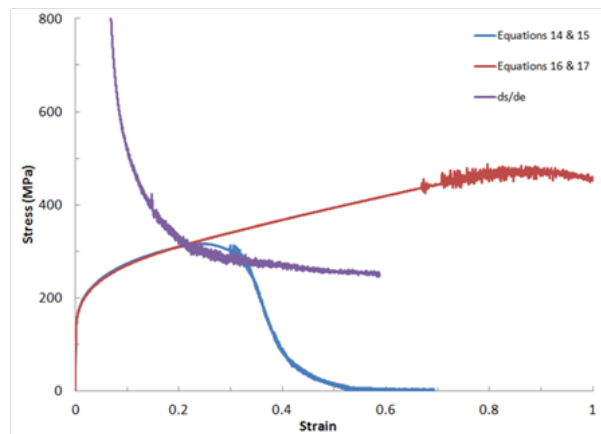


(c)

Figure 7: Stress vs. Strain for Abaqus Simulations.



(a)



(b)

Figure 8: Stress vs. Strain for Presto Simulations.

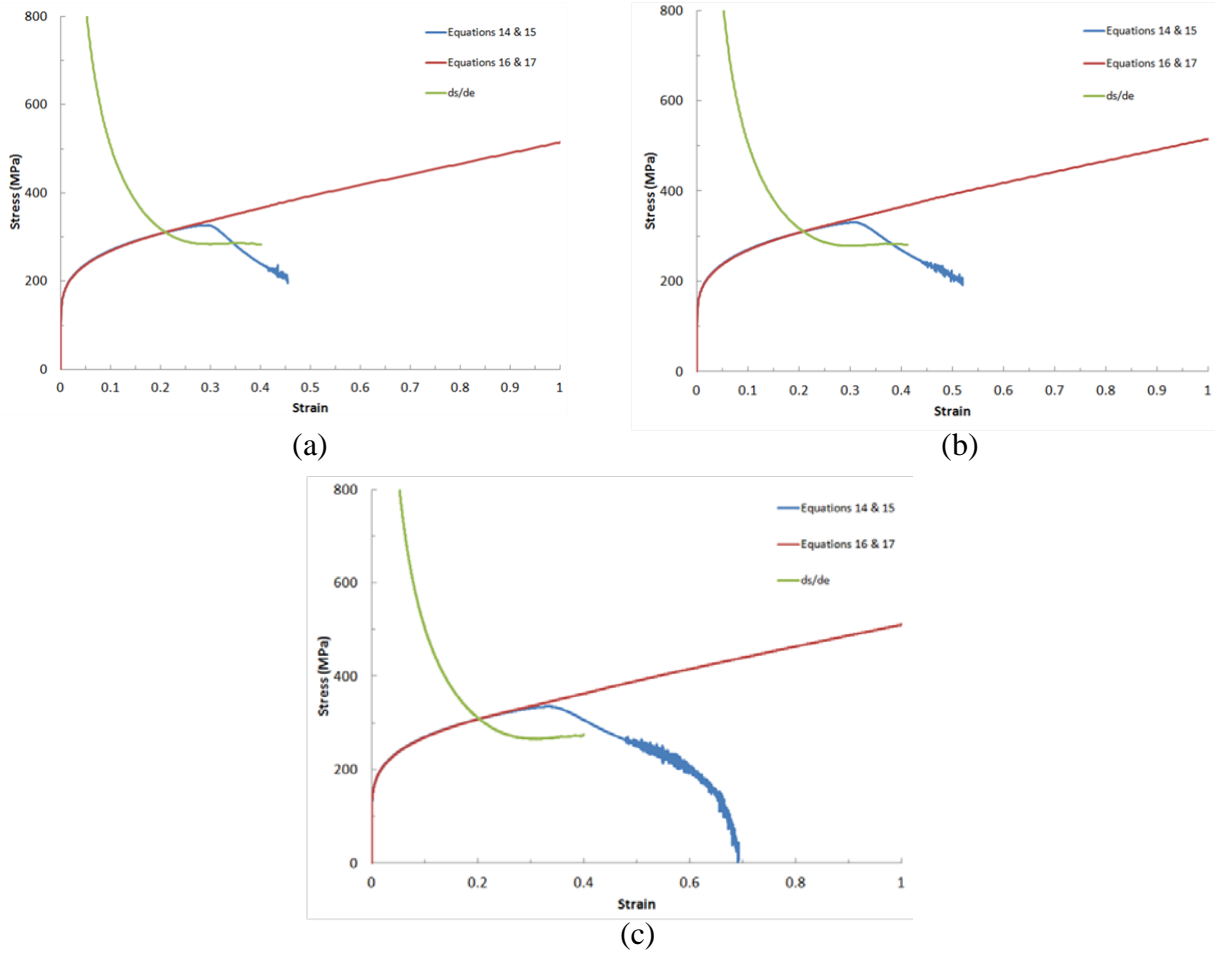


Figure 9: Stress vs. Strain for EPIC Simulations.

Void coalescence is shown in Figure 10, where void screenshots were taken at 0% true strain and at 50% true strain from Abaqus Model 1 simulation and are compared with the tomography pictures from the experiment in Ref. [3]. The stretch of the voids from Abaqus simulation very closely matches the experimental pictures.

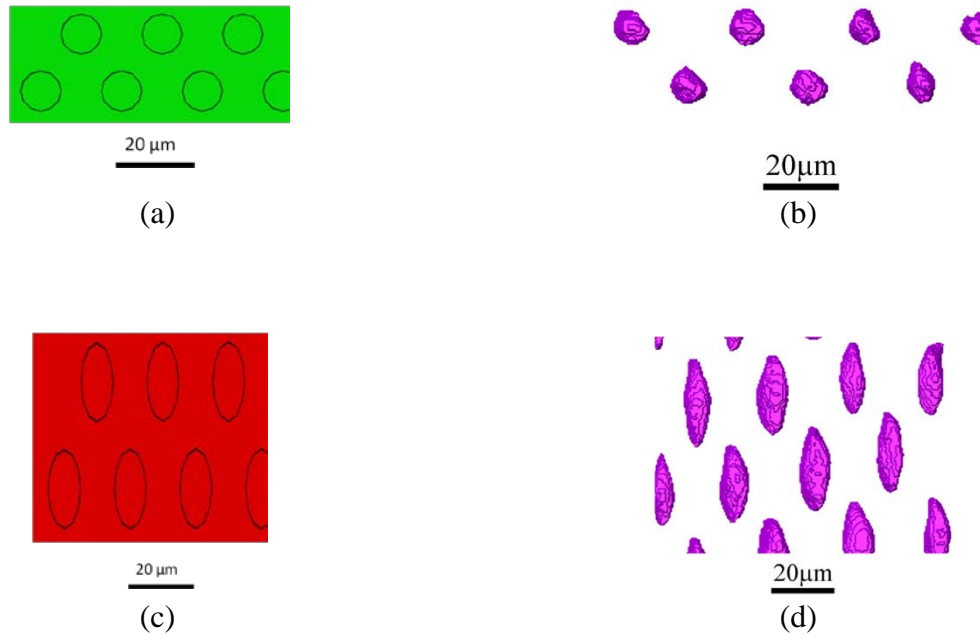


Figure 10: Abaqus Void Visualization vs. Experiment at 0% True Strain in (a) and (b), and at 50% True Strain in (c) and (d)

5.0 CONCLUSIONS

OFHC Copper material properties from the EPIC material library were used for all simulations. The true stress at necking for all simulations was found to be around 60-70 MPa higher than the experiment from Ref. [3] as Figure 6 shows. This seems to indicate that the simulations are not capturing the elastic response of the material accurately and the material model used in the simulations therefore does not match the material properties of the specimen tested in Ref. [3]. In order to test the codes capability of predicting void coalescence and failure more accurately, the material model should be first calibrated with an experimental test with no voids present in the specimen. Once the material model is accurate, then the computational simulations for the specimen with voids will compare more realistically with experimental results.

It was seen in this work that the best mesh to use this study would be Model 2. This is based on the consideration that the Abaqus simulation was 0.71% ϵ_n error and 0.60% σ_n from fully converged solutions based on the mesh convergence results, and that, for the EPIC simulations, the errors were 1.39% for ϵ_n and 0.26% for σ_n . Use of Model 2 is advised over Model 1 since the Abaqus simulation run time for Model 2 is 73% faster than for Model 1 and the EPIC simulation the run time for Model 2 is 49% faster than for Model 1.

The effects of element deletion were not closely studied in these simulations; however, it should be mentioned here that the deletion criteria for the Abaqus simulations was purely specified by the Johnson-Cook material failure model, while in the Presto and EPIC simulations, an equivalent plastic strain failure of 300% was specified as an additional deletion criteria. As far

as studying the number of deleted elements with changing mesh refinement, there is not data available from these simulations.

Note that all three codes produced such very similar results that we cannot base a comparison of prediction capability on these results alone. If run times are considered as a metric to judge the codes' performance, then Abaqus achieves the fastest run times out of the three.

6.0 REFERENCES

- [1] A. L. Gurson, "Continuum Theory of Ductile Rupture by Void Nucleation and Growth: Part I -- Yield Criteria and Flow Rules for Porous Ductile Media," *Journal of Engineering Materials and Technology*, vol. 9, pp. 2-15, 1977.
- [2] J. F. Kalthoff, "Modes of Dynamic Shear Failure in Solids," *International Journal of Fracture*, vol. 101, no. 1-2, pp. 1-31, 2000.
- [3] A. Weck, D. Wilkinson, E. Maire and H. Toda, "Visualization by X-Ray Tomography of Void Growth and Coalescence Leading to Fracture in Model Materials," *Acta Materialia*, vol. 56, no. 12, pp. 2919-2928, 2008.
- [4] D. L. Tonks, A. K. Zurek and W. R. Thissell, "Void Coalescence Model for Ductile Damage," in *Proc. 12th APS Topical Conference on Shock Compression of Condensed Matter - 2001*, Atlanta, GA, 2002.
- [5] J. Kim, X. Gao and T. S. Srivatsan, "Modeling of Void Growth in Ductile Solids: Effects of Stress Triaxiality and Initial Porosity," *Engineering Fracture Mechanics*, vol. 71, no. 3, pp. 379-400, 2004.
- [6] D. Lassance, F. Scheyvaerts and T. Pardoen, "Growth and Coalescence of Penny-Shaped Voids in Metallic Alloys," *Engineering Fracture Mechanics*, vol. 73, no. 8, pp. 1009-1034, 2006.
- [7] Y. Hammi and M. F. Horstemeyer, "A Physically Motivated Anisotropic Tensorial Representation of Damage with Separate Functions for Void Nucleation, Growth, and Coalescence," *International Journal of Plasticity*, vol. 23, no. 10, pp. 1641-1678, 2007.
- [8] E. Maire, O. Bouaziz, M. Di Michiel and C. Verdu, "Initiation and Growth of Damage in a Dual-Phase Steel Observed by X-Ray Microtomography," *Acta Materialia*, vol. 56, no. 18, pp. 4954-4964, 2008.
- [9] C. Landron, E. Maire, O. Bouaziz, J. Adrien, L. Lecarme and A. Bareggi, "Validation of Void Growth Models Using X-Ray Microtomography Characterization of Damage in Dual Phase Steels," *Acta Materialia*, vol. 59, no. 20, pp. 7564-7573, 2011.

- [10] J. R. Rice and D. M. Tracey, "On the Ductile Enlargement of Voids in Triaxial Stress Fields," *Journal of the Mechanics and Physics of Solids*, vol. 17, no. 3, pp. 201-217, 1969.
- [11] Y. Huang, "Accurate Dilatation Rates for Spherical Voids in Triaxial Stress Fields," *Journal of Applied Mechanics*, vol. 58, no. 4, pp. 1084-1086, 1991.
- [12] L. Siad, M. O. Ouali and A. Benabbes, "Comparison of Explicit and Implicit Finite Element Simulations of Void Growth and Coalescence in Porous Ductile Materials," *Materials & Design*, vol. 29, no. 2, pp. 319-329, 2008.
- [13] S. Ha and K. Kim, "Void Growth and Coalescence in F.C.C. Single Crystals," *International Journal of Mechanical Sciences*, vol. 52, no. 7, pp. 863-873, 2010.
- [14] AIAA, "Guide for the Verification and Validation of Computational Fluid Dynamics Simulations," American Institute of Aeronautics and Astronautics, AIAA-G-077-1998, Reston, VA, 1998.
- [15] K. M. Hanson and F. M. Hemez, "Uncertainty Quantification of Simulation Codes Based on Experimental Data," in *Proc. 41st Aerospace Sciences Meeting and Exhibit*, Reston, VA, 2003.
- [16] R. W. Logan and C. K. Nitta, "Comparing 10 Methods for Solution Verification, and Linking to Model Validation," *Journal of Aerospace Computing, Information, and Communication*, vol. 3, no. 7, pp. 354-373, 2006.
- [17] F. M. Hemez, J. S. Brock and J. R. Kamm, "Non-linear Error Ansatz Models in Space and Time for Solution Verification," in *Proc. 1st Non-deterministic Approaches (NDA) Conference and 47th AIAA/ASME/ASCE/AHS/ASC Structures, Structural Dynamics, and Materials (SDM) Conference*, 2006.
- [18] P. J. Roache, "Conservatism on Steady-State Fluid Flow and Heat Transfer," *Journal of Fluids Engineering*, vol. 125, no. 4, pp. 731-733, 2003.
- [19] D. J. Reding and S. Hanagud, "Code Verification for Energetic Structural Material Simulations," *AIAA Journal*, vol. 47, no. 7, pp. 1617-1626, 2009.
- [20] P. J. Roache, *Verification and Validation in Computational Science and Engineering*, Albuquerque, NM: Hermosa Publishers, 1998.
- [21] V. Tvergaard and A. Needleman, "Analysis of the Cup-Cone Fracture in a Round Tensile Bar," *Acta Metallurgica*, vol. 32, no. 1, pp. 157-169, 1984.
- [22] G. R. Johnson and S. R. Beissel, "Modular Material Model Subroutines for Explicit Lagrangian Computer Codes," Army Research Laboratory, ARL-CR-556, 2004.

- [23] *ABAQUS Analysis User's Manual, Version 6.9*, Pawtucket, RI: HKS, 2010.
- [24] SNL, "Presto 4.14 User's Guide," Sandia National Laboratories, SAND2009-74012, Albuquerque, NM, 2009.
- [25] G. R. Johnson, S. R. Beissel, C. A. Gerlach and T. J. Holmquist, "User Instructions for the 2011 Version of the EPIC Code," Southwest Research Institute, 2011.
- [26] D. J. Benson, "Computational Methods in Lagrangian and Eulerian Hydrocodes," *Computer Methods in Applied Mechanics and Engineering*, vol. 99, no. 2, pp. 235-394, 1992.
- [27] T. J. Holmquist, G. R. Johnson and W. H. Cook, "A Computational Constitutive Model for Concrete Subjected to Large Strain Rates and High Pressures," in *Proc. Fourteenth International Symposium on Ballistics*, Quebec City, Canada, 1993.

DISTRIBUTION LIST

AFRL-RW-EG-TR-2013-080

DEFENSE TECHNICAL INFORMATION CENTER - 1 Electronic Copy
ATTN: DTIC-OCA (ACQUISITION)
8725 JOHN J. KINGMAN ROAD, SUITE 0944
FT. BELVOIR VA 22060-6218

AFRL/RWOR (STINFO Office) - 1 Electronic Copy

ARDEC (1 Electronic Copy Each)

MICHAEL R. HESPOS
RDAR-MEE-M
BLDG.60
PICATINNY ARSENAL, NJ 07806

STEPHEN L. LUCKOWSKI
RDAR-MEE-P
BLDG.3150
PICATINNY ARSENAL, NJ 07806

STACEY L. KERWIEN
RDAR-MEE-M
BLDG.60
PICATINNY ARSENAL, NJ 07806

ADELPHI (1 Electronic Copy Each)

TUSIT WEERASOORIYA
RDRL-WMP-B
BLDG. 4600
ABERDEEN PROVING GROUNDS, MD 21005

BRYAN A. CHEESEMAN
RDRL-WMM-B
BLDG.4600
ABERDEEN PROVING GROUNDS, MD 21005

ANY OTHER INTERNAL AGENCIES THE DIVISION WISHED TO RECEIVE THE REPORT